Accepted Manuscript

Lumen-intima and media-adventitia segmentation in IVUS images using supervised classifications of arterial layers and morphological structures

Lucas Lo Vercio, Mariana del Fresno, Ignacio Larrabide

PII: S0169-2607(18)31822-4
DOI: https://doi.org/10.1016/j.cmpb.2019.05.021
Reference: COMM 4930

To appear in: *Computer Methods and Programs in Biomedicine*

Received date: 20 December 2018
Revised date: 26 April 2019
Accepted date: 20 May 2019

Please cite this article as: Lucas Lo Vercio, Mariana del Fresno, Ignacio Larrabide, Lumen-intima and media-adventitia segmentation in IVUS images using supervised classifications of arterial layers and morphological structures, *Computer Methods and Programs in Biomedicine* (2019), doi: https://doi.org/10.1016/j.cmpb.2019.05.021

Highlights

- Fully-automatic segmentation method for LI and MA in IVUS images
- It matchs and improves state-of-the-art fully-automatic segmentation methods.
- Modular open-source implementation that can be extended and improved is provided.

Lumen-intima and media-adventitia segmentation in IVUS images using supervised classifications of arterial layers and morphological structures

Lucas Lo Vercio[a,b], Mariana del Fresno[a,c], Ignacio Larrabide[a,b]

[a]*Pladema Institute, UNCPBA, Gral. Pinto 399, Tandil, Argentina*
[b]*Consejo Nacional de Investigaciones Científicas y Técnicas (CONICET), Argentina*
[c]*Comisión de Investigaciones Científicas de la Provincia de Buenos Aires (CICPBA), Argentina*

Abstract

Background: Intravascular ultrasound (IVUS) provides axial grey-scale images of blood vessels. The large number of images require automatic analysis, specifically to identify the lumen and outer vessel wall. However, the high amount of noise, the presence of artifacts and anatomical structures, such as bifurcations, calcifications and fibrotic plaques, usually hinder the proper automatic segmentation of the vessel wall.

Methods: Lumen, media, adventitia and surrounding tissues are automatically detected using Support Vector Machines (SVMs). The classification performance of the SVMs vary according to the kind of structure present within each region of the image. Random Forest (RF) is used to detect different morphological structures and to modify the initial layer classification depending on the detected structure. The resulting classification maps are fed into a segmentation method based on deformable contours to detect lumen-intima (LI) and media-adventitia (MA) interfaces.

Results: The modifications in the layer classifications according to the presence of structures proved to be effective improving LI and MA segmentations. The proposed method reaches a Jaccard Measure (JM) of 0.88±0.08 for LI segmentation, compared with 0.88±0.05 of a semiautomatic method. When looking at MA, our method reaches a JM of 0.84±0.09, and outperforms previous automatic methods in terms of HD, with 0.51mm±0.30.

Email address: lucaslovercio@conicet.gov.ar (Lucas Lo Vercio)

Conclusions: A simple modification to the arterial layer classification produces results that match and improve state-of-the-art fully-automatic segmentation methods for LI and MA in 20MHz IVUS images. For LI segmentation, the proposed automatic method performs accurately as semi-automatic methods. For MA segmentation, our method matched the quality of state-of-the-art automatic methods described in the literature. Furthermore, our implementation is modular and open-source, allowing for future extensions and improvements.

Keywords: IVUS, lumen-intima, media-adventitia, SVM, Random Forest, deformable contours

---

1. Introduction

Coronary disease and stroke are one of the leading causes of death in the world [1]. Blood flow in low caliper arteries, such as coronary and cerebral ones, can be reduced due to stenosis. This syndrome is called atherosclerosis, and it is produced by the presence of intimal hyperplasia, cholesterol and fibrous tissue [2]. Size and morphology statistics of the lumen-intima (LI) and media-adventitia (MA) contours provide information about the degree of atherosclerosis.

In the late 80s, intravascular ultrasound (IVUS) was developed providing, for the first time, axial images of the vascular lumen, vessel wall and sourrunding tissues [3]. Considering that IVUS imaging systems provide 25-30 frames per second, and the catheter is pulled back at 0.5-1 mm/s, IVUS series contain a large number of images. Automatic analysis of IVUS images becomes helpful for physicians, by providing automatic assessment of atherosclerosis and stenosis, as well as anatomical reconstruction for treatment planning and assessment [4, 5, 6]. Nevertheless, the automatic segmentation of arterial contours, a critical step for quantification and/or 3D reconstruction, remains a challenging problem due to the current approaches do not perform on par with expert observers [7, 8].

1.1. Related work

IVUS image quality is affected by speckle noise, typical for ultrasound images. Noise reduction and tissue enhacement in IVUS images have been tackled using different approaches. Noise-reduction filters, such as median

filter [9], nonlinear filtering [10] and anisotropic diffusion [11, 12], were previously applied to IVUS images for LI and MA segmentation. Although textural analysis is frequently used for plaque characterization [13, 14], textural descriptors were also considered for segmentation. For LI segmentation, textural descriptors derived from Gray Level Co-occurrence Matrixes (GLCM) were used in Pujol et al. [15], and Law's textural features were applied in Mendizabal-Ruiz et al. [16]. Ciompi et al. [17] used Local Binary Patterns (LBP) and Gabor Filters for MA segmentation. Using sequential feature selection and Support Vector Machines (SVMs), Lo Vercio et al. [18] demonstrated that the combination of despeckling filters and GLCM-based features is more effective than using only one feature group for lumen and arterial wall segmentation.

Detection of morphological structures, such as bifurcations and different kinds of atherosclerotic plaques, is an important step for IVUS segmentation, as they can interfere with LI and MA detection [19]. Detection of bifurcations has been performed using thresholding [10], and machine learning based classifiers [20]. Shadows, associated with calcifications and the guidewire artifact, were recognized using thresholding [21, 10, 22], cumulative mean [11, 17], among other techniques. Lo Vercio et al. [23] showed that shadows, bifurcations and echogenic plaques can be jointly detected by effectively combining several of the studied features using a Random Forest (RF) classifier. Furthermore, this detection was done independently from LI and/or MA segmentation, in contrast with existing approaches [22, 17].

Katouzian et al. [19] stated that the comparison between different methods was difficult because there was no publicly available dataset containing sufficient data for different morphological structures. Taki et al. [22] also approached this problem but did not consider the presence of large calcifications or bifurcations that can interfere with the segmentation. Gao et al. [7] and Su et al. [24] retrieved images from patients with moderate atherosclerosis, small calcifications and soft plaques, but also neglected bifurcations and hard plaques. In 2011, the challenge "Lumen + External Elastic Laminae Border Detection in IVUS" was introduced at the MICCAI 2011 Computing and Visualization for (Intra)Vascular Imaging (CVII) workshop, and an annotated dataset containing images with bifurcations, shadows and different sizes of plaques was made available [25]. The challenge led to the development of several semi- and fully-automatic segmentation methods using this dataset [26, 27, 28].

The publicly available dataset contains two subsets of IVUS images: one

with 435 images obtained at 20 MHz, and other with 77 images, captured using a 40 MHz transducer. The different frequencies generate images with different axial resolutions, penetrations and speckle patterns [29]. These characteristics prevent automatic methods from efficiently segmenting images captured using different equipment. [19].

In previous works we assessed the effectiveness for IVUS segmentation of different image features and structure presence indicators for 20 MHz images [18, 23]. The performance of the proposed SVM- and RF-based classifiers is a consequence of the feature selection processes and automatic computation of proper thresholds. However, the techniques were developed independentely of any contour segmentation method, and their positive impact on such methods was not assessed before.

According to the literature reviews of ultrasound segmentation written by Katouzian et al. [19] and, more recently, by Meiburger et al. [30], deformable contours or *snakes* are one of the most popular techniques. Particularly for IVUS segmentation, Taki et al. [22] used geometric deformable contour for LI and MA segmentation in single frames. Helical active contours were used by Jourdain et al. [31] to segment LI on IVUS series. Zhu et al. [32] incorporated gradient vector flow to the deformable model to detect LI and MA. In Zakeri et al. [33], MA segmentation was performed via dynamic directional vector field convolution active contour model. These proposed methods assessed their effectiveness in different datasets, some of them not containing all of the cited morphological structures. Furthermore, some of the proposals did not segment the entire vessel wall, but only the inner layer [31, 26], or outer layer [33, 17].

1.2. Contributions

In a previous work, Lo Vercio et al. [18] proposed a SVM-based fuzzy-classification of lumen, vessel wall, and surrounding tissues in structure-free IVUS images. Then, Lo Vercio et al. [23] used a RF to detect morphological structures, such as shadows, bifurcations and echogenic plaques, in IVUS images.

In this work, we combine, for the first time, these supervised classifiers into a deformable contour model for segmenting LI and MA. An edge map for each interface is generated from the SVM-based fuzzy classifications. These edge maps are modified according to the existing morphological structures, which are detected using a RF. Then, ellipses are fitted to approximate each

Table 1: Distribution of the dataset provided by Balocco et al. [25] and the number and percentage of columns in the polar images having each structure.

Set	**Number of frames/ number of columns**	**Columns**			
		No structure	**Bifurcation**	**Shadow**	**Echogenic Plaque**
Training set	109/55,808	49,786 (89.2%)	456 (0.8%)	666 (1.2%)	4,900 (8.8%)
Test set	326/166,912	133,850 (80.2%)	2,163 (1.3%)	8,197 (4.9%)	22,702 (13.6%)
Total	**435/222,720**	**183,636**	**2,619**	**8,863**	**27,602**

interface of the arterial wall. Finally, these curves are adjusted using deformable contours. We demonstrate that a general workflow can efficiently perform for both LI and MA segmentation, in contrast to methods found in the literature that use different strategies for each contour [17, 26]. Furthermore, it improves results of joint segmentation methods [27, 25].

The proposed method is evaluated using the publicly available dataset of 20 MHz IVUS images, which contains sufficient annotated images to perform a valid training-test scheme. Furthermore, it allows the comparison with state-of-the-art methods, showing improved results.

The modular workflow allowed us to assess the effectiveness of each step in the segmentation process, particularly the sensitivity to the presence of morphological structures and the effectiveness of our proposal to overcome this presence. The design of the method allows its extension and improvement, and its open-source implementation can be found at `https://github.com/lucaslovercio/IVUSprocessing`.

This article is organized as follows: Section 2 describes the classifiers and training, as well their combination in the deformable contour model. Section 3 provides the experimental results. Section 4 discuss these results, comparing them with related works in the field. Finally, Section 5 concludes the paper and identifies avenues for future works.

2. Materials and methods

2.1. IVUS images

We used the publicly available dataset of IVUS images provided by Balocco et al. [25], which comprises 435 images from 10 series, 384×384 sized, acquired using Si5 imaging system and a 20MHz Eagle Eye catheter (Volcano Corporation, California, USA). Annotations of LI and MA interfaces were also provided. The dataset was separated in 109 images for training and 326 for testing (Table 1).

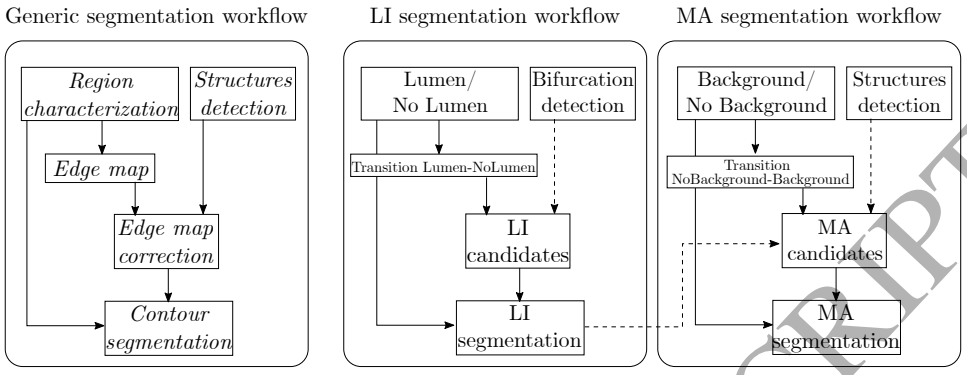

Figure 1: Workflows of the proposed IVUS segmentation method. Left: Generic workflow for a contour segmentation. Center: Lumen-intima segmentation workflow. Right: Media-adventitia segmentation workflow. Dashed lines represent flows of data to deal with structures.

IVUS images were transformed to polar coordinates [10, 34], resulting in 512×173 sized images where each column corresponds to a radial sample of the probe.

The polar images of the training set were labelled according to the provided annotations. Pixels above LI were marked as *Lumen*, and pixels below MA were labelled as *Background*. An IVUS expert categorized each column as bifurcation (B), shadow (S) or echogenic plaque (EP) [18, 23]. Table 1 depicts the number of columns for each structure.

2.2. Proposed segmentation method

The proposed method for LI and MA segmentation on IVUS is based on a highly decoupled workflow (Fig. 1). Initially, a pixel classification belonging to *Lumen* and *Background* regions is performed using a linear classifier, produced by SVM. Then, morphological structures are detected using RF, separately from the pixel classification. A candidate edge is placed in the transition between the resulting regions. Because of the presence of structures, the edge map must be modified to erase any anomalies produced by these structures. Finally, a contour segmentation is performed using the resulting score and edge maps.

LI and MA segmentations, which are described in the coming subsections, follow this generic workflow. Dashed arrows in Fig. 1 represent the actions which possibly improve the segmentations in presence of structures,

by modifiying the edge maps. Particularly, LI can be used to delete spurious candidates of MA.

2.3. Region characterization

The LI interface separates *Lumen* and *No Lumen* regions. In the same way, the MA interface separates *No Background* and *Background*. The pixels likelihood of belonging to a region is computed using SVMs, one for *Lumen/No Lumen* separation and other for *Background/No Background*.

To classify the previous regions, efficient combinations of image features were used. Maximum smoothed intensity [10], original image, and angular second moment [35] were considered to classify *Lumen/No Lumen*. For *Background/No Background* classification, the SVM was trained using maximum smoothed intensity, original image, median filtered image, distance from catheter [36], inverse difference moment [35] and shadow indicator [17]. In both cases, the SVM provided by the VLFeat library was trained using a linear kernel, L2-loss and $\lambda = 0.0001$ [37, 38], with 15 images from the training set without morphological structures (not containing B, S, or EP), according to Lo Vercio et al. [18]. Fig. 2 has examples of image classification using the resulting hyperplanes of the SVMs. Fig. 2a shows an image with echogenic plaque and shadows, and Fig. 2d depicts an image having a bifurcation. The resulting score map of these images show misclassifications in regions where structures are present.

2.4. Morphological structures detection

Columns of the polar image can present morphological structures such as bifurcations, shadows, echogenic plaques, or none of these (marked as N).

Shadows are produced when the ultrasound beam cannot be propagated through a material, such as the catheter guidewire or an atherosclerotic plaque composed by calcium (calcification). Shadows prevent the observation of the arterial wall, and may cause segmentation methods to fail.

In bifurcations, the arterial wall is not present. However, in the expert annotations of the ground truth, LI and MA are marked in bifurcation regions. Thus, fully or semi- automatic methods must infer the interfaces in these regions as the observer.

EP and adventitia have similar composition, resulting in similar echogenicity [17]. Consequently, EP can interfere in media-adventitia segmentation in gradient-based methods.

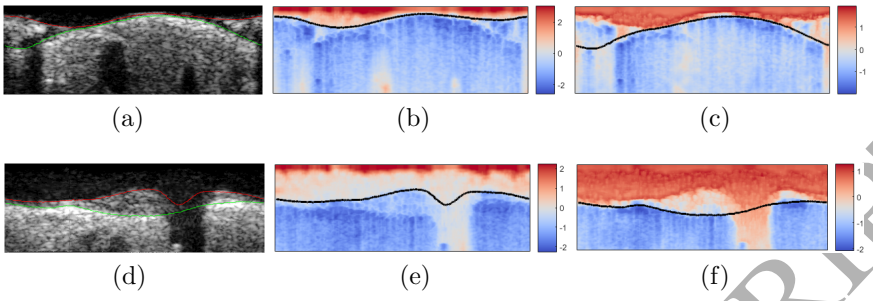

Figure 2: *Lumen/No Lumen* and *Background/No Background* characterization. (a) and (d) IVUS polar image and manual segmentation. LI marked in red, MA marked in green. (b) and (e) *Lumen/No Lumen* characterization for (a) and (d), respectively. Pixels classified as *Lumen* marked in shades of red, while classified as *No Lumen* marked in shades of blue [39]. LI marked in black. (c) and (f) *Background/No Background* characterization for (a) and (d), respectively. Pixels classified as *No Background* marked in shades of red, while the classified as *Background* marked in shades of blue. MA marked in black.

Consequently, the segmentation method must be trained taking into account these structures to provide successful results.

2.4.1. Random Forest classifier

To detect the mentioned structures in polar coordinates, the intensity profile of each column was characterized using twenty two descriptors:

- mean and standard deviation
- minimum and maximum of the column
- total radial energy [11]
- graytone variance among columns
- relative graytone [10]
- shadow and relative shadow indicators [17]
- median and standard deviation below maximum [21, 22]
- ratio between maximum and the column behind it [40]
- two minima and two maxima gradients [10]

- sum of these minima and maxima gradients
- number of positive pixels using Otsu's thresholding [21]
- slope, intercept and loss of a linear fitting

Random Forest was selected to classify each column using the listed descriptors, based on its ability to deal with multiclass and imbalanced problems in association with Random Undersampling (RUS) [41, 42, 43]. Columns labelled as N predominate over those having structures as it can be seen in Table 1. For balancing the training set of columns $(55,808)$, it was resampled by applying a RUS to N, to 15% of its original number. RFs had 100 trees and the number of descriptors randomly selected for each split was set to $\lfloor log_2 22 \rfloor$[23].

2.5. Contour segmentation

Deformable contours or *snakes* were used to segment LI and MA interfaces. They are widely used for medical image segmentation, particularly IVUS images [19]. The model consists of a closed parametric curve $X(u,v) = (x(u,v), y(u,v))$ that is iteratively deformed by the action of internal and external forces.

The evolution of each node of X from time t to $t + \Delta t$ is defined as

$$X_i^{t+\Delta t} = X_i^t - \frac{\Delta t}{\gamma}(a\alpha_i^t + b\beta_i^t - q\rho_i^t - pf_i^t) \tag{1}$$

where α_i and β_i are the local stretching and bending forces at X_i, respectively[44]. Parameter a weights the stretching, while b weights the local curvature. ρ is the inflation force, and f is the edge attracting force. The last two are called external forces, which will be explained in following subsections. Iterations stop when X achieves a steady state ($X^t = X^{t+\Delta t}$), or the maximum number of iterations is reached.

As the region classifications and the structure detection are performed on polar coordinates, the contours are also segmented in this space. One node of X per column is fixed. Then, having the polar image height h and width w, $X(0) = X(w-1)$ is defined to ensure a closed contour. Furthermore, the displacement of X_i is limited to column i. Thus, a node can only go up or down, changing its vertical position y $(0 \leq y \leq h-1)$.

2.5.1. Internal forces

The stretching force, which describes local distance between the nodes of the curve, is defined in polar coordinates as

$$\alpha_i = (X_i - X_{i-1}) + (X_i - X_{i+1}). \tag{2}$$

Arterial tissues are soft and present rounded interfaces among them. Thus, an appropriate value of the parameter a should be determined to ensure softened segmented interfaces.

The bending force represents the local curvature of the contour. Arterial tissues are concentric to the lumen and, therefore, they are concave in the cartesian space. The polar space imposes a constraint to the curve, ensuring concavity when it is transformed to cartesian space. Then, the bending coefficient b can be set to 0 [45].

2.5.2. External forces

Lumen/No Lumen scores are used as the external force ρ to segment LI. In the same way, *Background/No Background* scores are used for MA segmentation.

The external force f_i, which attracts X to the candidate edge, is constructed as follows: as LI is placed in the transition from *Lumen* region to *No Lumen* region, pixels in the transition *Lumen-No Lumen* are marked as positive in an edge map P_{LI} (Fig. 3). Likewise, MA can be found in *No Background-Background* transition. Pixels in this transition are marked in an edge map P_{MA}. It is worth noting that, when a process is applied to both edge maps, these are generically referred to P. Then, f_i is defined as a gaussian gradient G_σ with standard deviation σ:

$$f_i = \nabla[G_\sigma * P]. \tag{3}$$

2.5.3. Modification of the edge map

P must be modified to avoid the presence of false candidate edges produced by morphological structures. First, as the arterial contours are continous, maybe presenting some missing sections, a filter of connected components is performed to erase isolated points in P [32].

Lumen-No Lumen or *No Background-Background* transitions are not observed in bifurcations (Fig. 2e and 2f). Then, positive points in P located at bifurcations should be set to zero.

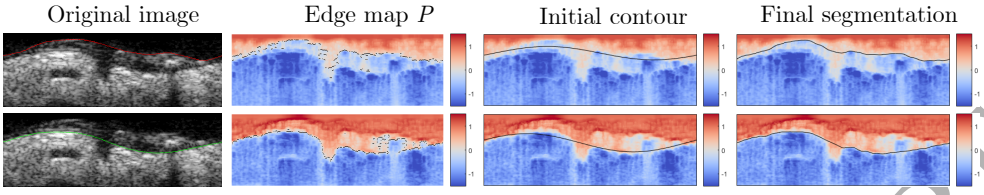

Figure 3: Step-by-step LI and MA segmentation. LI marked in red and MA marked in green, both interfaces retrieved from the annotation of the dataset. Score maps for *Lumen/No Lumen* and *Background/No Background* are depicted using the smooth cool warm colormap [39].

Shadows can interfere with the segmentation of both arterial contours. In the actual dataset, calcifications produce shadows, which hinder the observation of MA, but not LI (Fig. 2a). They affect *Background/No Background* scores, as it can be seen in Fig. 2c, where misclassified pixels as *Background* are observed over the MA. Furthermore, *No Background-Background* transition is not observed close to this contour. Thus, positive points in P_{MA} must be set to zero where shadows are detected.

In presence of echogenic plaque, both contours can be observed; nevertheless, misclassifications in the plaque region appear in the *Background/No Background* scores (Fig. 2c). Unlike shadows, *No Background-Background* transitions are still present (Fig. 3). Then, two or more transitions are observed in the columns of P_{MA} that have EP [10]. Segmentation algorithms must deal with such ambiguities. The proposed method sets to zero the positive points in P_{MA} which are in columns where the RF detected EP, and are inside of a 20 pixels radius of the segmented LI interface (Fig. 1).

2.5.4. Contour initialization

An initial contour needs to be provided for the deformable contour presented in Equation 1. For all the positive points in each column in P, the median value of the coordinate y is computed. The curve $g(i) = a_0 + a_1 cos(2\pi i/w) + b_1 sin(2\pi i/w)$, which is an ellipse in the cartesian space, is fitted to those median values [16, 27]. Then, the initial contour is $X = g(0)..g(w-1)$ (Fig. 3).

2.6. Metrics

For evaluating differences between the ground truth (GT) and the automatic segmentation (Auto), Hausdorff Distance (HD), Jaccard Measure

(JM) and Percentage of Area Difference (PAD) were used as suggested by Balocco et al. [25]. Before these computations, X is transformed to cartesian coordinates.

HD measures the maximum distance between the manual annotated contour $\mathrm{C_{GT}}$ and the automatic segmented contour $\mathrm{C_{Auto}}$ [46]. $e()$ is the minimum euclidean distance between node C_{1k} from C_1 and C_2:

$$e(\mathrm{C}_{1k}, \mathrm{C}_2) = \min_{j \in \mathrm{C}_2} \|\mathrm{C}_{1k} - \mathrm{C}_{2j}\|. \tag{4}$$

Then, HD is defined as:

$$\mathrm{HD}(\mathrm{C_{GT}}, \mathrm{C_{Auto}}) = \max\left(\max_{j \in \mathrm{C_{GT}}} e(\mathrm{C}_{\mathrm{GT}j}, \mathrm{C_{Auto}}), \max_{l \in \mathrm{C_{Auto}}} e(\mathrm{C}_{\mathrm{Auto}l}, \mathrm{C_{GT}}) \right). \tag{5}$$

JM computes the superposition between the region marked by the observed $\mathrm{R_{GT}}$ and the automatic segmented region $\mathrm{R_{Auto}}$:

$$\mathrm{JM}(\mathrm{R_{GT}}, \mathrm{R_{Auto}}) = \frac{\mathrm{R_{GT}} \cap \mathrm{R_{Auto}}}{\mathrm{R_{GT}} \cup \mathrm{R_{Auto}}}. \tag{6}$$

Thus, JM = 1 when regions perfectly match, and JM = 0 when the regions are not overlapped.

PAD computes the relative area difference between GT ($\mathrm{A_{GT}}$) and Auto ($\mathrm{A_{Auto}}$)

$$\mathrm{PAD}(\mathrm{A_{GT}}, \mathrm{A_{Auto}}) = \frac{|\mathrm{A_{GT}} - \mathrm{A_{Auto}}|}{\mathrm{A_{GT}}}. \tag{7}$$

When PAD = 0, both regions have the same area. To compute JMs and PADs in this work, the catheter region is excluded from R and A, respectively.

3. Results

3.1. Workflow and parameters configuration

The proposed contour algorithm (Section 2.5) has parameters to be determined: the tension coefficient a, the external force coefficients q and p, the standard deviation σ of the gaussian gradient, the time step Δt and the maximum number of iterations. The goal is to determine a set of parameters that maximizes the metrics. According to Equation 1, one parameter can

Table 2: Results from different configurations of the proposed workflow for segmenting LI and MA, evaluated in the training set. Means and standard deviations for HD, JM and PAD. p-values for the Wilcoxon signed rank test with null hypothesis: the median metric of segmentations with certain configuration is equal to the median of the metric obtained for a different configuration.

	LI			**MA**		
	HD	**JM**	**PAD**	**HD**	**JM**	**PAD**
(1) Region characterization	-	0.81(0.13)	0.19(0.36)	-	0.88(0.09)	0.07(0.09)
(2) Initial fitted curve	0.41(0.30)	0.81(0.14)	0.15(0.31)	0.29(0.24)	0.89(0.09)	0.07(0.09)
(3) Deformable contours	0.27(0.11)	0.91(0.03)	0.06(0.05)	0.29(0.23)	0.92(0.08)	0.05(0.07)
Wilcoxon Test vs (1)	$p < 0.001$	$p < 0.001$	$p = 0.11$	$p = 0.29$	$p < 0.001$	$p = 0.001$
(4) Initial fitted curve on the modified edge maps	0.42(0.30)	0.81(0.14)	0.15(0.31)	0.22(0.07)	0.93(0.02)	0.03(0.03)
Wilcoxon Test vs (2)	$p = 0.87$	$p = 0.94$	$p = 0.92$	$p = 0.003$	$p < 0.001$	$p < 0.001$
(5) Deformable contours with modified edge maps	0.28(0.11)	0.91(0.03)	0.06(0.05)	0.19(0.07)	0.94(0.03)	0.02(0.02)
Wilcoxon Test vs (3)	$p = 0.99$	$p = 0.99$	$p = 0.99$	$p < 0.001$	$p = 0.049$	$p = 0.049$

be fixed and the remaining coefficients must be determined experimentally. Thus, $p = 1$ was fixed. $\sigma = 2.5$, $\Delta t = 0.1$ and $200,000$ as the maximum number of iterations were also selected. Optimal values of a and q were determined via grid search for LI and MA segmentation using the 109 images of the training set. The highest JM, PAD and HD for LI were reached when $a = 3$ and $q = 0.5$. For MA, best results were obtained using $a = 0.3$ and $q = 0.0005$.

For analyzing the best configuration of the proposed workflow, Table 2 shows the values of the metrics when segmenting the training set: Region characterization based on SVMs (Section 2.3), initial fitted curve (Section 2.5.4), and the final segmentation using deformable contours (Section 2.5). Furthermore, statistical analysis using the Wilcoxon signed rank test is shown, to assess the improvement of applying the structure detection and edge maps modifications (Section 2.5.3).

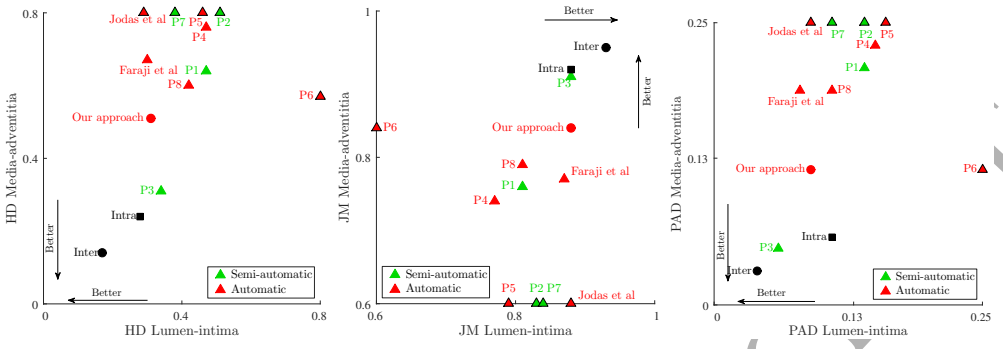

Figure 4: Reported Hausdorff Distance (HD), Jaccard Measure (JM) and Percentage of Area Difference (PAD) for the test set by the participants (P) in the IVUS segmentation challenge and by current approaches. Results of state-of-the-art methods are shown with triangles, being the semiautomatic ones marked in green, while automatic methods are shown in red. Intra- and inter-observer variability are depicted in black. Participants on an edge do not segment the correspondant interface.

3.2. Quantitative results

The proposed structure detection and treatment improved the segmentation using deformable contours, according to Table 2. With this configuration of the workflow, the 326 images of the test set were segmented. Table 3 includes the mean values of HD, JM and PAD, disaggregated by the presence of structures, without and with the edge modification step for analysis purposes. For this separation, it was defined that an image have B or S if at least 2% of the columns are marked as one of these structures. For EP, this proportion was set to 8%. Also, an image can have more than one structure. Furthermore, Table 3 shows the results for a cross validation, using 9 series for training of the RF, SVM and snake parameters, and one series for validation.

For comparison with state-of-the-art methods, Fig. 4 graphically depicts JM, HD and PAD values reported by Balocco et al. [25] and by current approaches also evaluated on the same set [26, 27].

3.3. Qualitative results

Fig. 5 depicts the manual annotations and the automatic segmentations when the method does not take action on morphological structures. Also, it

Table 3: Means and standard deviations for HD, JM and PAD of the proposed method, evaluated on the 326 images of the test set, dissagregated by the presence of structures. Images can present more than one structure. Metrics obtained without and with the edge modification step are shown in italics and normal font, respectively. In the last row, metrics from the cross-validation leaving one serie out, using the entire dataset, are also reported.

Set	**LI**			**MA**		
	HD	**JM**	**PAD**	**HD**	**JM**	**PAD**
Test set	*0.32(0.25)*	*0.88(0.08)*	*0.09(0.10)*	*0.57(0.31)*	*0.83(0.10)*	*0.13(0.09)*
(326 images)	0.31(0.25)	0.88(0.08)	0.09(0.10)	0.51(0.30)	0.84(0.09)	0.12(0.09)
None	*0.29(0.16)*	*0.89(0.05)*	*0.07(0.07)*	*0.38(0.24)*	*0.89(0.06)*	*0.06(0.05)*
(53 images)	0.30(0.16)	0.89(0.05)	0.07(0.07)	0.39(0.25)	0.88(0.08)	0.08(0.07)
Bifurcation	*0.44(0.33)*	*0.84(0.09)*	*0.12(0.13)*	*0.68(0.34)*	*0.79(0.12)*	*0.15(0.11)*
(49 images)	0.43(0.33)	0.84(0.09)	0.12(0.13)	0.69(0.42)	0.79(0.11)	0.17(0.13)
Shadow	*0.28(0.19)*	*0.87(0.06)*	*0.07(0.07)*	*0.67(0.36)*	*0.77(0.12)*	*0.16(0.11)*
(121 images)	0.28(0.19)	0.87(0.06)	0.07(0.07)	0.56(0.33)	0.80(0.10)	0.15(0.12)
Echogenic Plaque	*0.31(0.27)*	*0.88(0.09)*	*0.09(0.11)*	*0.61(0.29)*	*0.81(0.11)*	*0.14(0.09)*
(218 images)	0.31(0.27)	0.88(0.09)	0.09(0.11)	0.51(0.28)	0.84(0.09)	0.12(0.09)
10-fold cross validation	0.32(0.10)	0.88(0.04)	0.09(0.05)	0.53(0.22)	0.85(0.08)	0.11(0.08)

shows the SVM-based *Lumen/No Lumen* and *Background/No Background* classification, structure detection performed by the RF, and segmentation performed with the modified edge maps (Section 2.5.3). Fig. 5a is an image without structures, while Fig. 5b-(d) are images containing morphological structures.

4. Discussion

Fig. 4 shows that the mean value of JM for LI segmentation (0.88) outperforms participant automatic methods in the challenge ($0.77 - 0.81$), and it performs equal to the best semiautomatic one (0.88). Furthermore, recent methods for segmenting LI reach the same value. The observed value of HD (0.31) is lower than all the participants in the challenge ($0.34 - 0.51$), and slightly higher than recent approaches ($0.29 - 0.30$)[26, 27].

For MA segmentation, the proposed method performs as the best automatic method in the competition (P6) when comparing JM, and it has lower HD (0.51 vs. 0.57). It can be seen in Fig. 4 that our approach is the fully-automatic method closest to intra- and inter-observer variability. Thus, using the same strategy to segment both contours (Section 2.2), the proposed method segments LI and MA jointly as well as state-of-the-art methods which segment them separately [17, 26].

4.1. Sensitivity to structures

Table 3 shows that LI segmentation is affected by the presence of structures, when their mean JM, HD and PAD are compared with N. Particularly, images with B have the lowest mean JM (0.84) compared with the other categories ($0.87 - 0.89$). A similar conclusion can be inferred inspecting HDs, where images with B have higher HD than N, S and EP. Also, inspecting Fig.4 and, according to the conclusions of Balocco et al. [25], methods that detect B (ie. our approach, Jodas et al. [26]) perform better than those that do not take action on B. Qualitatively, Fig. 5b shows that LI segmentations differ from the ground truth in the bifurcation region. Accurate LI segmentations, in presence of EP and S, can be seen in Fig. 5c and 5d.

For MA segmentation, the three structures affect the performance of the algorithm, according to Table 3. It shows that the mean JM for B, S and EP is less than the mean JM for N. Fig. 5a shows that the segmentation method for MA performs well for images without structures, even when RF misclassify arterial regions as EP and S. In Fig. 5d the curve does not

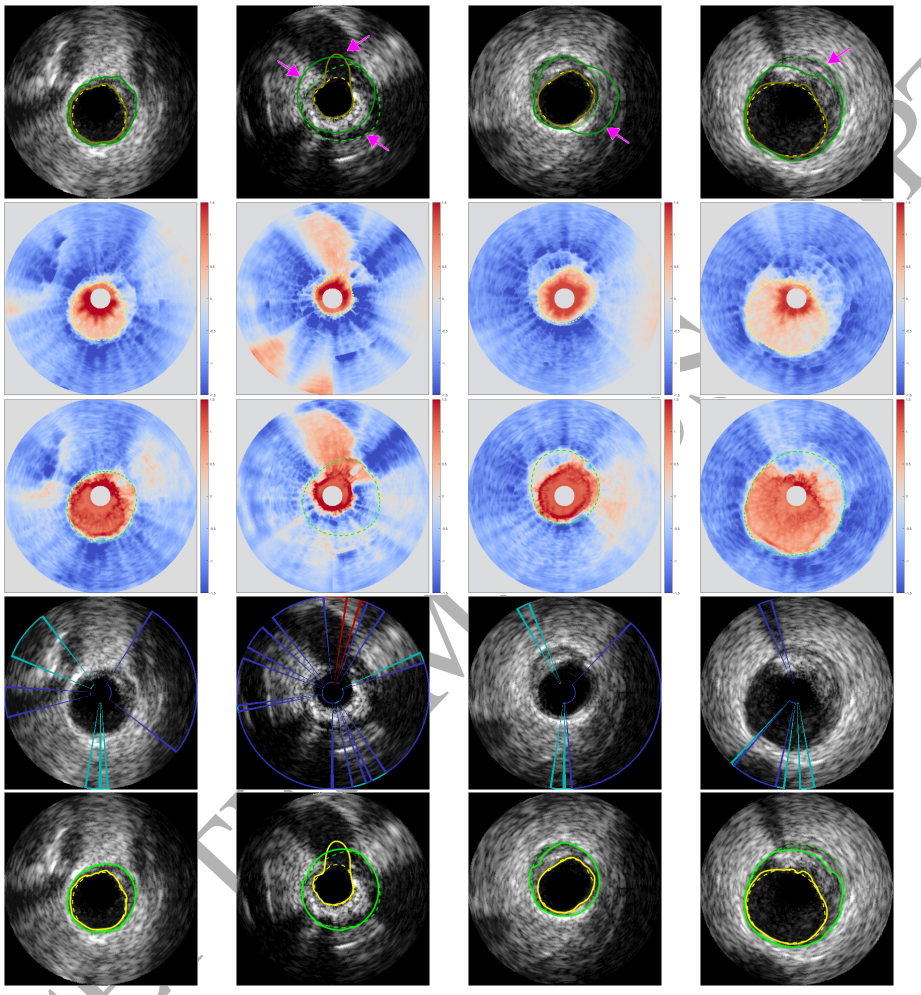

(a) (b) (c) (d)

Figure 5: Segmentation of IVUS images. LI marked in yellow and MA marked in green. GTs drawn in dashed lines, algorithm results in full lines. First row: images segmented without structure detection. Arrows point segmentation failures. Second row: *Lumen/No Lumen* classification. Third row: *Background/No Background* classification. Fourth row: structures detected (cyan=EP, red=B, blue=S). Fifth row: images segmented according to the presence of structures.

reach the marked MA when no structure detection is performed. When the structures are detected and the proposed corrections of the edge map are performed (Section 2.5.3), the segmentation is closer to the ground truth. For an image presenting echogenic plaque, the structure detection and corrections improve the segmentation, even when the RF confuses S and EP (Fig. 5b). Fig. 4 shows that methods which consider the presence of structures for MA segmentation (P6, our approach) perform better than those which do not take them into account (ie. Faraji et al. [27]).

4.2. Workflow analysis

Table 2 depicts metrics for different configurations of the proposed workflow (Fig. 1), evaluated on the training set. It shows that the pixel likelihood for *Lumen* and *No Background*, obtained by SVMs, have JMs higher than 0.8. When comparing these results to those reported in the literature (Fig. 4b, reported for the test set), fuzzy classification seems to be a good starting point for any contour segmentation method, even when the SVMs are trained using structure-free images but evaluated on images presenting structures.

The initial curve for the deformable contour method and the refined contour can be analyzed. It is shown in row **(2)** of Table 2 that the ellipse fitting equalizes or improves the metrics of the SVM classification. Then, the refinement via deformable contours substantially improves the metrics, with JM around 0.9 (Table 2 - row **(3)**). For lumen segmentation, this improvement can be related to the presence of eccentric plaque, which provokes a non-elliptical lumen shape [47]. These results confirm that the proposed SVMs likelihoods are useful for LI and MA segmentation.

Taking into account the presence of vascular structures and LI segmentation, the effectiveness for MA segmentation significantly increases, reaching a mean JM higher than 0.91 in the training set (Table 2 - row **(5)**). Also, the contour refinement via *snakes* still performs better than the ellipse fitting. These results show that detecting and considering the structures is an important step for MA segmentation.

Table 3 shows similar trends as Table 2 when the test set is segmented without and with the segmentation step. As theoretically expected, the obtained metrics in the test set are not good as in the training set. However, particularly in the presence of EP and S when segmenting MA, it is shown that the structure detection and treatment step improves the results. Thus, inspecting Fig. 4, the proposed method outperforms methods that do not detect structures [22, 24, 27].

4.3. Extensibility

Image features designed for IVUS image analysis have been considered previously. However, it has been demonstrated, particularly for Random Forests, that the classifiers can be improved when features learned by convolutional neural networks (CNN) are included [48]. Consequently, the effectiveness of the classifiers can be enhanced by considering CNN features, both trained with IVUS images and transferred from other domains.

Classification scores obtained by SVMs for *Lumen* and *Background* classifications [18] can be included, i.e., as unary potentials in graph-based methods [49, 50] and in holistic segmentation techniques [17]. Also, segmentation modules (curve fitting and *snake* method) can be replaced with techniques already used for IVUS segmentation, such as fast-marching [51, 52] and region-growing [7], among others.

The proposed framework, particularly the pixel and structure classification, is based on machine learning techniques. Therefore, their effectiveness can be enhanced by using larger datasets. At this time, it is worth noting that a limitation for the current training-test scheme is the proportion for training and test in the dataset. The recommended proportion is 70% for training and 30% for testing [53], but the publicly available dataset used already 25% for training (Table 1). Using a leave-one-serie-out validation scheme for training, it is shown in the last row of Table 2 that PAD and JM are improved compared to the first row. However, a direct comparison with other methods, such as in Fig. 4, is not valid because they use a different test set.

Finally, the modular design of the workflow, shown in Fig. 1, and the availability of the source code, allow the implementation of these proposed improvements and the reuse of the modules by the research community.

5. Conclusions

A fully-automatic method for vessel wall segmentation in 20 MHz IVUS images was presented. It was assessed that the detection of echogenic plaques, bifurcations and shadows, and the proper modification of the layers classifications improves state-of-the-art results. As classification modules are based on machine-learning techniques, such as Support Vector Machines and Random Forest, they can be improved by using a larger dataset of IVUS images. Finally, the extensibility and possible improvements of the method were dis-

cussed, and they are supported by the availability of the open-source code (`https://github.com/lucaslovercio/IVUSprocessing`).

Acknowledgements

This project is partly funded by PICT 2014-1730 and PICT 2016-0116 - FONCYT - ANPCYT of Argentina. L. L. is supported by CONICET postdoctoral grant. The financial support of these institutions is greatly appreciated.

Conflict of interest

The authors declare that there are no conflicts of interest in this work.

References

[1] A. Go, D. Mozaffarian, V. Roger, E. Benjamin, J. Berry, W. Borden, D. Bravata, S. Dai, E. Ford, C. Fox, S. Franco, H. Fullerton, C. Gillespie, S. Hailpern, J. Heit, V. Howard, M. Huffman, B. Kissela, S. Kittner, D. Lackland, J. Lichtman, L. Lisabeth, D. Magid, G. Marcus, A. Marelli, D. Matchar, D. McGuire, E. Mohler, C. Moy, M. Mussolino, G. Nichol, N. Paynter, P. Schreiner, P. Sorlie, J. Stein, T. Turan, S. Virani, N. Wong, D. Woo, M. Turner, Heart disease and stroke statistics-2013 update: A report from the american heart association, Circulation 127 (2013).

[2] X. Zhang, C. R. McKay, M. Sonka, Tissue characterization in intravascular ultrasound images, IEEE Transactions on Medical Imaging 17 (1998) 889–899.

[3] S. E. Nissen, J. C. Gurley, C. L. Grines, D. C. Booth, R. McClure, M. Berk, C. Fischer, A. N. DeMaria, Intravascular ultrasound assessment of lumen size and wall morphology in normal subjects and patients with coronary artery disease., Circulation 84 (1991) 1087–1099.

[4] F. Weichert, H. Mller, U. Quast, A. Kraushaar, P. Spilles, M. Heintz, C. Wilke, C. von Birgelen, R. Erbel, D. Wegener, Virtual 3D IVUS vessel model for intravascular brachytherapy planning. I. 3D segmentation, reconstruction, and visualization of coronary artery architecture and orientation, Medical Physics 30 (2003) 2530–2536.

[5] J. A. Noble, D. Boukerroui, Ultrasound image segmentation: a survey, Medical Imaging, IEEE Transactions on 25 (2006) 987–1010.

[6] F. Ciompi, S. Balocco, J. Rigla, X. Carrillo, J. Mauri, P. Radeva, Computer-aided detection of intracoronary stent in intravascular ultrasound sequences, Medical Physics 43 (2016) 5616–5625.

[7] Z. Gao, W. K. Hau, M. Lu, W. Huang, H. Zhang, W. Wu, X. Liu, Y.-T. Zhang, Automated framework for detecting lumen and media-adventitia borders in intravascular ultrasound images, Ultrasound in Medicine & Biology 41 (2015) 2001 – 2021.

[8] E. G. Mendizabal-Ruiz, I. A. Kakadiaris, A physics-based intravascular ultrasound image reconstruction method for lumen segmentation, Computers in Biology and Medicine 75 (2016) 19 – 29.

[9] R. Sanz-Requena, D. Moratal, D. R. García-Sánchez, V. Bodí, J. J. Rieta, J. M. Sanchis, Automatic segmentation and 3D reconstruction of intravascular ultrasound images for a fast preliminar evaluation of vessel pathologies, Comput Med Imaging Graph 31 (2007) 71–80.

[10] G. Unal, S. Bucher, S. Carlier, G. Slabaugh, T. Fang, K. Tanaka, Shape-driven segmentation of the arterial wall in intravascular ultrasound images, IEEE Trans Inf Technol Biomed 12 (2008) 335–347.

[11] D. Gil, A. Hernandez, O. Rodriguez, J. Mauri, P. Radeva, Statistical strategy for anisotropic adventitia modelling in IVUS, IEEE Trans Med Imaging 25 (2006) 768–778.

[12] T. Koga, E. Uchino, N. Suetake, Automated boundary extraction and visualization system for coronary plaque in IVUS image by using fuzzy inference-based method, in: Fuzzy Systems (FUZZ), 2011 IEEE International Conference on, pp. 1966–1973.

[13] V. G. Giannoglou, D. G. Stavrakoudis, J. B. Theocharis, V. Petridis, Genetic fuzzy rule based classification systems for coronary plaque characterization based on intravascular ultrasound images, Engineering Applications of Artificial Intelligence 38 (2015) 203 – 220.

[14] Y. N. Hwang, J. H. Lee, G. Y. Kim, E. S. Shin, S. M. Kim, Characterization of coronary plaque regions in intravascular ultrasound images

using a hybrid ensemble classifier, Computer Methods and Programs in Biomedicine 153 (2018) 83 – 92.

[15] O. Pujol, M. Rosales, P. Radeva, E. Nofrerias-Fernández, Intravascular ultrasound images vessel characterization using adaboost, in: I. E. Magnin, J. Montagnat, P. Clarysse, J. Nenonen, T. Katila (Eds.), Functional Imaging and Modeling of the Heart, volume 2674 of *Lecture Notes in Computer Science*, Springer Berlin Heidelberg, 2003, pp. 242–251.

[16] E. G. Mendizabal-Ruiz, M. Rivera, I. A. Kakadiaris, Segmentation of the luminal border in intravascular ultrasound B-mode images using a probabilistic approach, Med Image Anal 17 (2013) 649–670.

[17] F. Ciompi, O. Pujol, C. Gatta, M. Alberti, B. Simone, X. Carrillo, J. Mauri-Ferre, P. Radeva, HoliMAb: A holistic approach for media-adventitia border detection in intravascular ultrasound, Med Image Anal 16 (2012) 1085–1100.

[18] L. Lo Vercio, J. I. Orlando, M. del Fresno, I. Larrabide, Assessment of image features for vessel wall segmentation in intravascular ultrasound images, International Journal of Computer Assisted Radiology and Surgery 11 (2016) 1397–1407.

[19] A. Katouzian, E. D. Angelini, S. G. Carlier, J. S. Suri, N. Navab, A. F. Laine, A state-of-the-art review on segmentation algorithms in intravascular ultrasound (IVUS) images, IEEE Trans Inf Technol Biomed 16 (2012) 823–834.

[20] M. Alberti, S. Balocco, C. Gatta, F. Ciompi, O. Pujol, J. Silva, X. Carrillo, P. Radeva, Automatic bifurcation detection in coronary IVUS sequences, IEEE Trans Biomed Eng 59 (2012) 1022–1031.

[21] E. dos Santos Filho, Y. Saijo, T. Yambe, A. Tanaka, M. Yoshizawa, Segmentation of calcification regions in intravascular ultrasound images by adaptive thresholding, in: Computer-Based Medical Systems, 2006. CBMS 2006. 19th IEEE International Symposium on, pp. 446–454.

[22] A. Taki, Z. Najafi, A. Roodaki, S. Setarehdan, R. Zoroofi, A. Konig, N. Navab, Automatic segmentation of calcified plaques and vessel borders in IVUS images, Int J Comput Assist Radiol Surg 3 (2008) 347–354.

[23] L. Lo Vercio, M. del Fresno, I. Larrabide, Detection of morphological structures for vessel wall segmentation in IVUS using random forests, in: 12th International Symposium on Medical Information Processing and Analysis, volume 10160, pp. 1016012–1–10.

[24] S. Su, Z. Hu, Q. Lin, W. K. Hau, Z. Gao, H. Zhang, An artificial neural network method for lumen and media-adventitia border detection in IVUS, Computerized Medical Imaging and Graphics 57 (2017) 29 – 39.

[25] S. Balocco, C. Gatta, F. Ciompi, A. Wahle, P. Radeva, S. Carlier, G. Unal, E. Sanidas, J. Mauri, X. Carillo, T. Kovarnik, C.-W. Wang, H.-C. Chen, T. P. Exarchos, D. I. Fotiadis, F. Destrempes, G. Cloutier, O. Pujol, M. Alberti, E. G. Mendizabal-Ruiz, M. Rivera, T. Aksoy, R. W. Downe, I. A. Kakadiaris, Standardized evaluation methodology and reference database for evaluating IVUS image segmentation, Comput Med Imaging Graph 38 (2014) 70 – 90.

[26] D. S. Jodas, A. S. Pereira, J. M. R. Tavares, Automatic segmentation of the lumen region in intravascular images of the coronary artery, Medical Image Analysis 40 (2017) 60 – 79.

[27] M. Faraji, I. Cheng, I. Naudin, A. Basu, Segmentation of arterial walls in intravascular ultrasound cross-sectional images using extremal region selection, Ultrasonics 84 (2018) 356 – 365.

[28] D. China, P. Mitra, D. Sheet, On the fly segmentation of intravascular ultrasound images powered by learning of backscattering physics, in: N. Dey, A. S. Ashour, S. Borra (Eds.), Classification in BioApps: Automation of Decision Making, Springer International Publishing, 2018, pp. 351–380.

[29] F. Destrempes, M.-H. R. Cardinal, Y. Saijo, G. Finet, J.-C. Tardif, G. Cloutier, Assessment of inter-expert variability and of an automated segmentation method of 40 and 60 mhz IVUS images of coronary arteries, PloS one 12 (2017) e0168332.

[30] K. M. Meiburger, U. R. Acharya, F. Molinari, Automated localization and segmentation techniques for b-mode ultrasound images: A review, Computers in Biology and Medicine 92 (2018) 210 – 235.

[31] M. Jourdain, J. Meunier, J. Sequeira, G. Cloutier, J.-C. Tardif, Intravascular ultrasound image segmentation: A helical active contour method, in: Image Processing Theory Tools and Applications (IPTA), 2010 2nd International Conference on, pp. 92–97.

[32] X. Zhu, P. Zhang, J. Shao, Y. Cheng, Y. Zhang, J. Bai, A snake-based method for segmentation of intravascular ultrasound images and its in vivo validation, Ultrasonics 51 (2011) 181–189.

[33] F. S. Zakeri, S. K. Setarehdan, S. Norouzi, Automatic media-adventitia IVUS image segmentation based on sparse representation framework and dynamic directional active contour model, Computers in Biology and Medicine 89 (2017) 561–572.

[34] M.-H. R. Cardinal, G. Soulez, J.-C. Tardif, J. Meunier, G. Cloutier, Fast-marching segmentation of three-dimensional intravascular ultrasound images: A pre- and post-intervention study, Medical Physics 37 (2010) 3633–3647.

[35] R. Haralick, K. Shanmugam, I. Dinstein, Textural features for image classification, Systems, Man and Cybernetics, IEEE Transactions on SMC-3 (1973) 610–621.

[36] B. K. Courtney, A. L. Robertson, A. Maehara, J. Luna, K. Kitamura, Y. Morino, R. Achalu, S. Kirti, P. G. Yock, P. J. Fitzgerald, Effects of transducer position on backscattered intensity in coronary arteries, Ultrasound in Medicine & Biology 28 (2002) 81 – 91.

[37] A. Vedaldi, B. Fulkerson, VLFeat: An open and portable library of computer vision algorithms, 2008.

[38] S. Shalev-Shwartz, T. Zhang, Stochastic dual coordinate ascent methods for regularized loss, J Mach Learn Res 14 (2013) 567–599.

[39] K. Moreland, Diverging color maps for scientific visualization, in: G. Bebis, R. Boyle, B. Parvin, D. Koracin, Y. Kuno, J. Wang, R. Pajarola, P. Lindstrom, A. Hinkenjann, M. L. Encarnao, C. T. Silva, D. Coming (Eds.), Advances in Visual Computing, volume 5876 of *Lecture Notes in Computer Science*, Springer Berlin Heidelberg, 2009, pp. 92–103.

[40] D. Xing, F. Yang, J. Gao, X. Qiu, S. Tu, J. Dijkstra, Intravascular ultrasound image hard plaque recognition and media-adventitia border detection, in: M. Long (Ed.), World Congress on Medical Physics and Biomedical Engineering, Springer Berlin Heidelberg, Beijing, China, 2013, pp. 931–934.

[41] L. Breiman, Random forests, Machine Learning 45 (2001) 5–32.

[42] A.-L. Boulesteix, S. Janitza, J. Kruppa, I. R. Knig, Overview of random forest methodology and practical guidance with emphasis on computational biology and bioinformatics, Wiley Interdisciplinary Reviews: Data Mining and Knowledge Discovery 2 (2012) 493–507.

[43] D. J. Dittman, T. M. Khoshgoftaar, R. Wald, A. Napolitano, Comparison of data sampling approaches for imbalanced bioinformatics data, in: FLAIRS Conference, pp. 268–271.

[44] T. McInerney, D. Terzopoulos, T-snakes: Topology adaptive snakes, Medical Image Analysis 4 (2000) 73 – 91.

[45] H. L. Manterola, L. Lo Vercio, A. Díaz, M. del Fresno, I. Larrabide, Validation of an open-source tool for measuring carotid lumen diameter and intima–media thickness, Ultrasound in Medicine and Biology 44 (2018) 1873–1881.

[46] V. Chalana, Y. Kim, A methodology for evaluation of boundary detection algorithms on medical images, IEEE Transactions on Medical Imaging 16 (1997) 642–652.

[47] B. F. Waller, C. A. Pinkerton, J. D. Slack, Intravascular ultrasound: a histological study of vessels during life. The new 'gold standard' for vascular imaging., Circulation 85 (1992) 2305–2310.

[48] J. I. Orlando, E. Prokofyeva, M. del Fresno, M. B. Blaschko, An ensemble deep learning based approach for red lesion detection in fundus images, Computer methods and programs in biomedicine 153 (2018) 115–127.

[49] S. Sun, M. Sonka, R. R. Beichel, Graph-based IVUS segmentation with efficient computer-aided refinement, IEEE Transactions on Medical Imaging 32 (2013) 1536–1549.

[50] E. Essa, X. Xie, I. Sazonov, P. Nithiarasu, D. Smith, Shape prior model for media-adventitia border segmentation in IVUS using graph cut, in: B. H. Menze, G. Langs, L. Lu, A. Montillo, Z. Tu, A. Criminisi (Eds.), Medical Computer Vision. Recognition Techniques and Applications in Medical Imaging, Springer Berlin Heidelberg, 2013, pp. 114–123.

[51] F. Destrempes, M.-H. R. Cardinal, L. Allard, J.-C. Tardif, G. Cloutier, Segmentation method of intravascular ultrasound images of human coronary arteries, Computerized Medical Imaging and Graphics 38 (2014) 91 – 103.

[52] J. Yan, D. Lv, Y. Cui, A novel segmentation approach for intravascular ultrasound images, Journal of Medical and Biological Engineering 37 (2017) 386–394.

[53] E. Alpaydin, Introduction to Machine Learning. 2nd, The MIT Press, 2010.